CHAPTER 23

New Science Opportunities and Experimental Approaches enabled by High Repetition Rate Soft X-ray Lasers

R.W. Schoenlein[*], A. Aquila, D. Cocco, G. Dakovski, D.M. Fritz, J.B. Hastings, P.A. Heimann, T. Osipov, W. Schlotter

Linac Coherent Light Source, SLAC National Accelerator Laboratory, 2575 Sand Hill Rd., Menlo Park, CA 94025

*Corresponding contributor. E-mail: rwschoen@slac.stanford.edu

23.1 Introduction

We are in a golden age for X-ray light sources, with thousands of scientists routinely using X-ray beams at modern synchrotron facilities to answer fundamental questions in chemistry, physics, materials science, and biology. The recent development of X-ray lasers has initiated in a new era in X-ray science by providing coherent ultrafast X-ray pulses with unprecedented peak brightness. The first generation of these facilities (*e.g.* the FLASH facility at DESY Hamburg,[1] and the LCLS facility at SLAC[2]) have already had tremendous scientific impact, and numerous similar facilities are now in operation or are under constructions around the world.[3] However, despite their enormous peak brightness, the average X-ray brightness from these facilities is quite modest, comparable to or lower than that available from existing storage rings. This restricts their application in many important areas of science. This results from the fact that first-generation XFELs are based almost exclusively on pulsed-RF accelerator technology, which limits the achievable repetition rate.

A new generation of XFELs is now under development that will overcome this restriction by exploiting continuous-wave RF superconducting accelerator technology (CW-SCRF) to provide ultrafast X-ray pulses at high repetition rate (~MHz) in a uniform or programmable time structure. This development is driven by important new science opportunities that have been identified and advanced over the past decade through scientific workshops, both in the U.S. and

around the world. Most recently, a series of science workshops held at SLAC National Accelerator Laboratory in February 2015 focused on the new science opportunities[4] that will be enabled by the LCLS upgrade project (LCLS-II) which will provide ultrafast X-rays in the 0.25-5 keV range at repetition rates up to 1 MHz with two independent XFELs based on adjustable-gap undulators: 0.25-1.25 keV soft X-ray undulator (SXU) and 1-5 keV hard X-ray undulator (HXU).[5]

This chapter highlights a few of the important new science opportunities enabled by such a facility in the areas of: (1) fundamental charge and energy flow in molecular complexes, (2) photo-catalysis and coordination chemistry, (3) quantum materials, and (4) coherent imaging at the nanoscale. The examples in this chapter represent just a few of the many science opportunities where high repetition rate is particularly enabling, and is not intended to be comprehensive of the broad range of science to be done at such facilities. Some key new experimental methods enabled by high repetition rate are also described, and initial concepts and capabilities of new instrumentation being planned for the LCLS upgrade are outlined.

23.2 Fundamental Dynamics of Energy and Charge in Atoms and Molecules

Charge migration, redistribution and localization, even in simple molecules, are not well understood at the quantum level. These fundamental phenomena are central to complex processes such as photosynthesis, catalysis, and bond formation/dissolution that govern all chemical reactions. Charge migration and localization in molecules is a coordinated process of both electronic and atomic motion, and indirect evidence points to the importance of quantum coherences and coupled evolution of electronic and nuclear wave functions in many molecular systems. However, we have not been able to directly observe these processes to date, and they are beyond the description of conventional chemistry models. Ultrafast soft X-rays at high-repetition-rate from advanced XFELs will enable new dynamic molecular reaction microscope techniques that will directly map charge distributions and reaction dynamics in the molecular frame.

23.2.1 Dynamic molecular reaction microscope

Ultrafast soft X-rays at high-repetition-rate from advanced XFELs will provide qualitatively new

probes of excited-state energy and charge flow and how they work in simple and complex molecular systems. The high repetition rate will enable sophisticated coincidence measurement schemes for kinematically complete experiments at each time step of an evolving reaction. This experimental approach, known as a "molecular reaction microscope",[6, 7] measures simultaneously the momenta (energy and direction) of all the constituent components of a molecular complex, typically via pulsed ionization and spectroscopy of the charged fragments using position-sensitive time-of-flight (TOF) techniques with multiple detection channels for electrons, and ions or charged fragments (as illustrated in Fig. 23.1).

{Fig 23.1 near here}

Figure 23.1 Artist view of a molecular reaction microscope (also known as COLd Target Recoil Ion Momentum Spectroscopy, COLTRIMS). Only one molecule is in the X-ray beam on each pulse (i.e. less than one ionization event per pulse). The ion and electron momenta are fully characterized in coincidence via position-sensitive time-of-flight detectors (graphic courtesy of R. Dörner, Goethe U. Frankfurt).

Photoelectrons emitted from localized inner shell levels are powerful probes for "illuminating molecules from within".[6, 8] A photoelectron wave originating from a specific site in the molecule is scattered by the instantaneous molecular structure at the moment of photo absorption. Recording such photoelectron scattering patterns in coincidence with the momenta of the fragment ions enables the reconstruction of the molecule at a fixed orientation in space (and time). Figure 23.2 shows a recent example of the structure of a methane molecule in the stationary electronic ground state measured via coincidence techniques at a synchrotron source. Photoelectrons emitted from the C-1s shell clearly reflect the positions of the H atoms in the molecular reference frame.

{Fig 23.2 near here}

Figure 23.2 Methane (stationary electronic ground-state) imaged in the molecular frame via the K-shell photoelectron angular distribution. Top: Calculated photoelectron angular distribution integrated over all polarization directions. Bottom: The experimental photoelectron angular distribution obtained from the (H^+, H^+, CH^{+2}) decay pathway (from [9]).

The promise of high-repetition-rate XFELs is to advance these techniques to the time domain to follow molecular dynamics in the excited-state on fundamental time scales, using coincidence

techniques to identify molecules with a fixed orientation in space. In these applications, specific dynamics are initiated via tailored transient excitations such as: charge transfer, vibrational excitation, creation of a valence hole via ionization, creation of non-equilibrium Rydberg wavepackets, strong dressing fields etc. Recent XFEL experiments point toward promising opportunities for dynamic reaction microscope studies.[10-13] For example, studies of charge-transfer dynamics in gas-phase iodomethane[14] identified three dissociative channels based on the time-dependent kinetic energy distributions of the charged fragments and comparison with model calculations. Dynamic reaction microscope studies at high repetition rate will enable the complete spatial reconstruction of the excited-state charge transfer and subsequent dissociation at each time step for a fixed-in-space molecular orientation. This is a potentially powerful approach for visualizing a broad range of excited-state molecular dynamics from dissociation of simple diatomic molecules, to charge-transfer processes, to isomerization and ring-opening reactions,[15] to non-Born-Oppenheimer relaxation processes,[16] to quantum symmetry breaking processes that mediate the emergence of chirality.[17]

Some of the key instrumentation requirements to exploit high-repetition-rate X-ray pulses for dynamic molecular reaction microscope studies include the following capabilities:

a) **Tuning range**: 0.25 to 1.2 keV. This spans the K-edges of critical light elements, C (284 eV), N (410 eV), O (543 eV) through the L-edges of the 3d transition metals.

b) **Beam focus**: ~300 nm diameter. Reaction microscopes operate with only one molecule in the X-ray beam per pulse. A small focus (short Rayleigh range) enables the use of higher density gas jet targets thus providing a well-defined spatial origin of the charged fragments to facilitate the spatial reconstruction of the reaction.

c) **Vacuum**: UHV ~10^{-11} Torr. This is essential to ensure that electrons and charged fragments originate only from molecules in the focal region by minimizing contributions from background gas along the X-ray beam path.

d) **Electron spectrometer:** Electric and magnetic fields collect electrons and ions over a 4π solid angle and project them to high-speed detectors (combination of micro-channel plates and delay-line) providing both position and time information (time-of-flight), ideally with multi-hit capability at rates >100 kHz.

e) **Lasers:** Provisions for tailored excitation spanning a broad spectral range from UV to

visible to THz at peak intensities of $>10^{12}$ W/cm^2, with synchronization to X-ray pulses at the <10 fs level.

23.2.2 Nonlinear X-ray Approaches for Mapping Valence Charge Dynamics

New nonlinear X-ray spectroscopies offer the potential to map charge flow and quantum coherences in an element-specific way for the first time. High repetition rate sources will be essential to realize the potential of these new approaches by enabling experiments in the perturbative regime which give rise to small nonlinear signals but also avoid the complications from higher-order nonlinearities and nonlinear wave propagation effects that arise in the strongly nonlinear regime.

The tremendous promise of nonlinear and multidimensional spectroscopy techniques in the X-ray region lies in the capability to follow coherent charge flow and energy relaxation on fundamental (attosecond to femtosecond) time scales with access to the full range of valence states (unrestricted by dipole selection rules). Importantly, the element specificity provided by X-rays (tuned to core-level absorptions) will enable us for the first time to follow charge and energy flow between constituent atoms in materials. These essential capabilities are not attainable using infrared or visible laser pulses, and will provide critical insight to correlated electron systems and molecular complexes with strong coupling between electronic and nuclear dynamics. Here we highlight two promising approaches: coherent or stimulated X-ray Raman spectroscopy (SXRS) for creating nonstationary electronic wavepackets localized on specific atoms,[18, 19] and X-ray core-hole correlation spectroscopy (XCCS) which probes the correlations between valence excited-states associated with different atomic sites in a molecule.[20, 21]

{Fig 23.3 near here}

Figure 23.3 Illustration of coherent or Stimulated X-ray Raman Spectroscopy (SXRS) in which localized valence excitations $|f_1>$ and $|f_2>$ are created and probed via resonant Raman processes at specific atoms. This approach creates a local valence excitation, and enables element-specific probing of charge flow.

Figure 23.3 illustrates coherent or stimulated X-ray Raman spectroscopy (SXRS). Whereas conventional optical Raman spectroscopy techniques exploit visible or infra-red laser fields to

probe lower-frequency vibrational resonances in matter, SXRS uses X-rays to probe valence electronic excitations in matter. One may consider SXRS as a powerful extension (stimulated or impulsive version) of spontaneous resonant inelastic X-ray scattering processes such a RIXS. The advantage of this approach is that it creates a localized valence excitation, or coherent electronic wavepacket, via a resonant transition originating from the core level of a specific atom (see Figure 23.3). A probe pulse in resonance with a second atom can then follow the time evolution of the wavepacket, and the flow of valence charge between different atomic sites, via various probe interaction mechanisms, for example: X-ray absorption spectroscopy, photoelectron spectroscopy, or via a second SXRS process (as illustrated in Figure 23.3).

{Fig 23.4 near here}

Figure 23.4 Excitation energy transfer simulation in Zn/Ni porphyrin heterodimer. The X-ray pump pulse is resonant with the Zn L_3-edge, and creates a localized valence excitation (wavepacket) via SXRS. Evolution of electron and hole densities (isosurfaces) are calculated from the non-stationary valence superposition states prepared via SXRS (adapted from ref. 19).

The potential impact of SXRS is illustrated in Figure 23.4, which shows recent SXRS simulations of ultrafast energy transfer dynamics in a Zn/Ni porphyrin heterodimer which are of interest as model components in artificial light harvesting and photosynthetic complexes.[19] In the simplest pump-probe implementation, a nonstationary valence electronic wavepacket (in the vicinity of an atom of interest) is created by two interactions with the field of a pump pulse resonant with a core transition. The delayed probe pulse (*e.g.* resonant with a core transition from a different atom) interacts with this wavepacket via a second Raman process, and the change in absorption reports on the dynamics of the wavepacket. Importantly, since the final state (from either the pump or probe pulse) is not core-excited, but only valence-excited, this approach accesses time scales that are much longer than the core-hole lifetime.

{Fig 23.5 near here}

Figure 23.5 Illustration of core-hole correlation spectroscopy in which resonant core-level excitation of two atoms is used to probe the coupling between their respective valence states f_1 and f_2.[20]

A complement to SXRS is X-ray core-hole correlation spectroscopy (XCCS) as illustrated in Fig.

23.5.[20-22] This approach is essentially the equivalent of two-dimensional electronic spectroscopy[22-24] but in the X-ray regime. It exploits nonlinear interactions with coherent X-ray pulses to probe correlation effects between pairs of valence electrons excited at different atomic sites in a molecule.

Figure 23.6 presents an example in which core-hole correlation spectroscopy probes the quantum coupling between nitrogen- and oxygen-associated valence states in different isomers of aminophenol. Here, two pulses probe the aminophenol molecule, one centered at 400 eV (ω_N) and the other at 535 eV (ω_O), in resonance with the N-1s and O-1s core excitations, respectively. In a coherent four-wave mixing implementation, the initial excitation is created by a pulse-pair, and a third pulse (in a phase-matched geometry) reads out the scattered Raman signal. Thus, XCCS measures a third-order, $\chi^{(3)}$, four-wave mixing process whereby a sequence of three incident pulses (three fields), $E_n(k_n, \omega_n)|_{n=1, 2, 3}$, generate a stimulated signal, e.g., $E_{sig}(-\omega_1+\omega_2+\omega_3)$, in the momentum-matched direction, $k_{sig}=-k_1+k_2+k_3$. The Fourier transform of the signal with respect to the time delays of the pulses creates a two-dimensional (2D) spectral map of the valence electronic structure. Off-diagonal features in this 2D map are present only when there is correlation between the two excited valence electrons on the N and O atoms; no signal should be seen in the Hartree-Fock limit of independent orbitals. Calculations show that the extent of this correlation depends not only on molecular structure (*i.e.*, it differs in ortho- and para-aminophenol), but also on the nature of the molecular orbitals excited within the energy envelopes (~10 eV) of ω_N and ω_O.[20, 21] An important criterion for core-level correlation spectroscopy is that the X-ray pulse durations must be faster than the Auger decay time (~5 fs[25]), since Auger decay suppresses the correlation signal of interest.

{Fig 23.6 near here}

Figure 23.6 Valence and core-excited states of aminophenols of *para* and *ortho* isomers of aminophenol, and the predicted corresponding 2D X-ray core-hole correlation maps. The off-diagonal cross-peaks (right map) indicate the quantum mixing between nitrogen- and oxygen-associated valence states (mixing of the N-1s and O-1s XANES spectra). Such quantum effects are absent in the para isomer due to the separation of the O and N atoms (adapted from ref. 20).

A rough estimate for the photon densities required for SXRS, XCCS and related nonlinear X-ray

science is based on typical absorptions cross-sections in the soft X-ray range, ~10^{-18} cm^2, which suggests that a fluence of >10^{17} ph/cm^2 is required. In the case of XCCS, the pulse duration must be comparable to (or less than) the order of the core-hole lifetime (~5 fs for for X-ray transitions[25]). This corresponds to >10^9 photons/pulse in a 1 μm focus (>10^{15} W/cm^2 at 500 eV). Estimates based on X-ray nonlinear susceptibilities lead to similar conclusions for the required X-ray peak power density.[18, 20] Note that modern nonlinear optical spectroscopy experiments typically operate in the perturbative regime, ~0.1 photons per cross-section, in order to avoid distortion of the spectral signal of interest from saturation, and other undesirable effects. In the case of SXRS, a coherent bandwidth of ~3 to 5 eV is required to couple to a manifold of valence states in order to create a localized wavepacket. This corresponds to a pulse duration of 0.36 to 0.6 fs at the Fourier transform limit, although SXRS may be tolerant to some degree of pulse chirp.

23.2.3 LCLS Instrument NEH 1.1

A new LCLS instrument, NEH 1.1,[26] is now under development to support the following areas of science: (1) fundamental dynamics of energy and charge as described above, as well as (2) quantum systems in strong fields, and (3) nanoscale structure and dynamics in matter via soft X-ray coherent imaging and scattering. The tuning range of NEH 1.1 will span from 0.25 to 2.5 keV covering the K-edges of critical light elements, C (284 eV), N (410 eV), O (543 eV) through the L-edges of the 3d transition metals, and extending into the tender X-ray range where an optimum balance is predicted between resolution and scattering cross-section for coherent X-ray imaging application.[27] The instrument will operate without a monochromator to support sub-fs and two-color operating modes of LCLS.[28, 29]

Instrument NEH 1.1 will support two endstations: DREAM (Dynamic REAction Microscope) and LAMP (named after the original LCLS-ASG-Michigan project). The new DREAM endstation will be optimized for dynamic reaction microscope studies with extreme vacuum, sub-micron X-ray focus, and target purity requirements dictated by pump-probe and coincidence detection at repetition rates in excess of 100 kHz. The projected X-ray fluence from the SXU source is ~10^{21} photons/cm^2 (*e.g.* at 700 eV) with the new CW-SCRF linac at high repetition rate, and ~10^{22} photons/cm^2 with the existing copper (Cu-RF) linac at 120Hz.[30]

LAMP is a highly flexible and modular endstation optimized for coherent forward scattering, small and wide angle scattering, diffraction and imaging. It will accommodate a variety of gas, liquid, and solid samples and will support a suite of established spectrometers including high resolution ion and electron time-of-flight (iTOF, eTOF) spectrometers, magnetic bottle, hemispherical analyser, velocity-map imaging (VMI) etc., in addition to the suite of LCLS X-ray imaging detectors. The projected X-ray fluence is ~10^{21} photons/cm^2 (*e.g.* at 700 eV) with the CW-SCRF linac, and ~10^{22} photons/cm^2 with the Cu-RF linac.[30]

23.3 Photo-catalysis and Coordination Chemistry

Understanding the fundamental processes of photo-chemistry is essential for directed design of photo-catalytic systems for chemical transformation and solar energy conversion that are efficient, chemically selective, robust, and based on earth-abundant elements. The central events of excited state chemistry critically influence the performance of photo-catalysts since stable charge separation, transport, and localization are mediated by internal conversion, intersystem crossing, and conformational changes on the ultrafast time scale. Understanding charge dynamics in molecular systems with strong interaction between electronic and nuclear structure, particularly for systems far from equilibrium, remains a significant challenge as these processes cannot be readily observed or calculated with standard experimental or theoretical methods.

Conventional chemistry models assume disparate time scales for evolution of electronic and atomic structure (Born-Oppenheimer approximation), but evidence points to the importance of coupled electronic/atomic structure (non-Born-Oppenheimer) in many systems. In materials and molecules with strong coupling between charge and vibrational modes, carriers trap in self-induced local distortions (conformational changes) and defects. The energetics and dynamics of these processes are critical to the photo-catalyst performance, but we lack the requisite tools to reliably disentangle the coupled motion of electrons and nuclei in many energy-critical materials. New tools that enable direct observation of these central events will qualitatively advance our understanding of chemical dynamics in photo-catalytic systems, and advance the development of design principles for directing molecular and materials synthesis.

The transition metal based Ru-Co donor-bridge-acceptor complex (shown in Fig. 23.7) illustrates these ideas that impact the performance of a diverse range of molecules and materials.[31] In this model photo-catalyst, metal-to-ligand-charge transfer (MLCT) excitations of the coordinated Ru cation efficiently harvest visible light. This initiates a series of ultrafast changes in electronic and nuclear structure (spanning tens of femtoseconds to several picoseconds) including: electron transfer, solvation between the distinct ligands coordinating the Ru and Co cations, and conversion of the optically-dark Co site from low-spin Co^{III} to high-spin Co^{II}. In principle, the oxidized Ru^{III} site and the reduced Co^{II} site can catalyze oxidation and reduction reactions. While the processes that follow photoexcitation have been identified, the sequence of events remains unclear, and we lack effective design rules for how to manipulate these processes through intra- and inter-molecular modifications.

{Fig 23.7 near here}

Figure 23.7 Non-equilibrium electron-transfer across the photoexcited ($^1Ru^{II}=^1Co^{III}$) model photo-catalyst. The fundamental timescales are indicated, as obtained from transient optical absorption spectroscopy (TOAS), X-ray emission spectroscopy (XES), and X-ray diffuse scattering (XDS).[31]

23.3.1 Excited-state charge dynamics via resonant inelastic X-ray scattering (RIXS)

Ultrafast soft X-rays at high-repetition-rate from advanced XFELs will enable powerful new methods for understanding and ultimately controlling, the physics and chemistry of photo-catalysis. Charge separation, charge transport, and catalysis are local phenomena. X-ray techniques can disentangle the coupled motion of electrons and nuclear dynamics with atomic resolution and chemical specificity, making them uniquely powerful for studying chemical dynamics. The new capabilities of LCLS-II will complement and significantly enhance the present attributes of LCLS – particularly for X-ray spectroscopy such as resonant inelastic X-ray scattering (RIXS) as shown in Fig. 23.8. RIXS measures the energy distribution of occupied and unoccupied molecular orbitals thus providing sensitivity to the local chemistry of a metal center with high resolution.

{Fig 23.8 near here}

Figure 23.8 Left: Resonant inelastic X-ray scattering (RIXS). Right: Time-resolved Fe L_3-RIXS maps (energy transfer vs. incident photon energy) of $Fe(CO)_5$ ground-state (top), and difference intensities for the time intervals 0-700 fs (middle) and 0.7-3.5 ps (bottom).[32]

Time-resolved RIXS at the femtosecond scale has recently been demonstrated at the LCLS where solution-phase studies of $Fe(CO)_5$ were combined with quantum chemical calculations to provide the first detailed mechanistic picture of frontier-orbital changes associated with the ligand photo-dissociation process (Fig. 23.8).[32] These studies of large structural changes on model molecular systems at high concentrations (~1 M) demonstrate the potential of time-resolved RIXS to correlate orbital symmetry with spin multiplicity and reactivity in short-lived reaction intermediates. However, the RIXS technique is currently still limited in data quality and not feasible for many interesting systems at lower concentration. With the dramatic increase in average brightness provided by high-repetition rate XFELs, RIXS with high spectral resolution and femtosecond time resolution will enable complete time-sequenced mapping of frontier orbital energies and subtle conformational changes that drive charge separation and transfer in complex functioning systems where the active sites are often in dilute concentrations.

23.3.2 LCLS Instrument NEH 2.2

A new LCLS instrument, NEH 2.2,[26] is now under development to support the following areas of science: (1) photo-catalysis and coordination chemistry as described above, (2) heterogeneous catalysis and interfacial chemistry, (3) nonequilibrium spin and magnetism at fundamental time scales, and (4) nanoscale electronic structure dynamics, heterogeneity, and fluctuations in materials. The tuning range of NEH 2.2 will span from 0.25 to 1.6 keV covering the K-edges of critical light elements, C (284 eV), N (410 eV), O (543 eV) through the L-edges of the $3d$ transition metals, and extending into the lanthanide $M_{4,5}$-edges. The instrument will be served by the SXU source followed by a monochromator with adjustable resolving power from R=10,000 to 50,000 at close to the Fourier transform limit. For example $\Delta E_{FWHM} = 100$ meV $\Leftrightarrow \Delta t_{FWHM} = 18$ fs (R=10,000 at 1 keV) or $\Delta E = 20$ meV $\Leftrightarrow \Delta t = 90$ fs (R=50,000 at 1 keV). NEH 2.2 will provide an adjustable focus from ~1 μm (horiz.) × 4 μm (vert.), compatible with high spectrometer resolution and micron-scale liquid jets, up to ~1 mm diameter for moderate spectrometer resolution, high throughput, and low incident fluence (ph/cm^2) as maybe required for delicate samples.

Instrument NEH 2.2 will incorporate a kinematic mounting scheme to accommodation of a wide range of specialized endstations supporting the following experimental capabilities:

a) Resonant coherent X-ray imaging and small angle X-ray scattering for studies of non-periodic materials, nano-structures, and domain dynamics (*e.g.* magnetization imaging and dynamics). This endstation will provide moderate vacuum (~10^{-7} torr) and will incorporate a forward scattering area detector with adjustable *q*-range suitable to access nanometer to micrometer length scales, and *in-situ* magnetic field capabilities.

b) Low-resolution spectroscopy (XAS, XES and RIXS) for studies of excited-state dynamics of condensed-phase molecules (predominantly solution environment): photo-catalysts, metallo-enzymes, and other bio-molecules. This endstation will accommodate both liquid jets and solid samples. A moderate resolution spectrometer (<500 meV) with large collection angle will provide high throughput.

c) Surface science, interfacial chemistry, heterogeneous catalysis and chemical dynamics via time-resolved photoelectron spectroscopy, absorption spectroscopy, and RIXS. This will be a UHV endstation with standard surface science instrumentation, molecular beam gas dosing for sample renewal and rapid sample translation. The RIXS spectrometer will be capable of mapping electronic excitations at 200 meV resolution with large collection angle.

d) Nanoscale and heterogeneous dynamics in correlated electron systems via resonant elastic scattering and soft X-ray photon correlation spectroscopy (XPCS). This UHV endstation (~10^{-8} torr) will accommodate solid samples with cryogenic temperature control and manipulation over 6-degrees of freedom, with an area detector that can be scanned over 90 degrees in elevation from the equator and azimuthally by 180 degrees from the direct beam.

23.4 Quantum Materials

"Quantum materials" refers broadly to solids that are not adequately described by single-electron band models or by reductionist approaches that consider only the constituent particles — individual atoms, electrons and their orbitals. Strong coupling between particles in quantum

materials gives rise to competing or entwined order, phase separation, and heterogeneity – including nanoscale texture of charge, spin and orbitals – that exhibit temporal and spatial fluctuations over many time and length scales and are intimately related to the macroscopic material properties. Interest in these materials stems in large part from powerful "emergent" properties such as high-temperature superconductivity, colossal magnetoresistivity, and topologically protected phases that arise from strong coupling effects.

The richness of quantum materials is illustrated in Fig. 23.9, which shows the influence of Coulomb interaction and the strength of the spin-orbit (SO) coupling on low-energy electronic states. Simple metals and semiconductors that are the mainstay of modern technology are materials in the weak-coupling region where conventional models satisfactorily explain the material properties. Quantum materials, however, reside outside this weak-coupling region, and understanding their rich electronic behaviour requires new concepts and new experimental approaches that provide direct insight to collective modes.

{Fig 23.9 near here}

Figure 23.9 Classification of materials via spin-orbit coupling and Coulomb interaction strength (adapted from [33]).

The $3d$ transition metal oxides, such as the high temperature (high-T_c) superconducting cuprates, are representative strongly-correlated electron systems (strong Coulomb interaction) where SO coupling is negligible in determining the low-energy electronic state (see for example ref. 34). In the strong SO coupling limit, the effects of topological order and quantum geometry[35, 36] have been extensively explored in topological insulators and transition metal dichalcogenides. Here conventional band structure models fail to capture the quantum geometry of the electronic wavefunctions, as embodied in the "Berry curvature" in momentum space (e.g. electric polarization and topological insulators) or in in real space (e.g. skyrmions and related particle-like spin textures).[37] There is now significant interest in understanding the role of SO coupling as an origin of new phenomena in strongly correlated materials.[38] For example, electron correlation can result in frustrated magnetic order and high-T_C superconductivity, while strong SO coupling can create a novel electronic structure that is topologically protected by quantum-geometrical constraints, leading to the tantalizing prospect of topologically protected superconductivity.

The two-particle, dynamic structure factor, $S_e(\boldsymbol{q},\omega) \sim \chi(\boldsymbol{q},\omega)$ represents a fundamental model for understanding an interacting electron system in terms of the charged collective modes. However, while the study of quasiparticles in quantum materials is now well advanced, we still lack an effective means to directly probe $S_e(\boldsymbol{q},\omega)$. Because the ground states of quantum materials arise from a subtle balance among competing interactions, the relevant collective modes appear at modest energy, typically 1 to 100 meV (see Fig. 23.10), where even modern X-ray sources and scattering spectrometers lack the required combination of photon flux and energy resolution. The absence of a means to measure ground-state collective modes – the essential observable of an interacting electron system – represents an enormous gap in our understanding of quantum materials. It is in this area that high repetition rate XFELs will offer transformative capabilities – for both characterizing ground-state collective modes (energy and momentum dependence across the Brillouin zone), and for following their response to tailored external stimuli.

{Fig 23.10 near here}

Figure 23.10 Left: Momentum transfer dependent resonant inelastic X-ray scattering (RIXS) probe of collective charge states. Right: Collective excitations that can be characterized by RIXS – including excitations within *d*-orbital manifolds (*d-d*) and charge-transfer excitations (CT). Higher resolution is essential to reveal collective excitations at energy scales comparable to that of superconducting gap and pseudogap $\sim k_B T$ (<25 meV) (image adapted from ref. 39).

23.4.1 Opportunities for momentum transfer dependent resonant inelastic X-ray scattering (RIXS) at XFELs

Unlike in the RIXS method used to study chemical dynamics, where the incident energy and the energy transfer are varied (see Section 23.3.1), the RIXS method applied to the study of quantum materials probes both the energy and momentum-transfer of scattered X-rays. This method, also sometimes referred to as qRIXS, is a powerful tool to map the energy-momentum dispersion of collective excitations.[40] Currently RIXS instruments routinely provide an energy resolution of ~100 meV (resolving power ~10,000), and have revealed a number of collective excitations in energy-momentum space, such as the dispersions of magnons,[41] paramagnons,[42] triplons,[43] two-spinons,[44] phonons,[45] and orbitons,[44] to name a few. State-of-the art RIXS instruments (*e.g.* ESRF ID32,[46] NSLS-II 2-ID SIX[47]) provide a resolving power greater than 30,000 with $\sim 10^{12}$ ph/s on sample (or R~100,000 at $\sim 10^{11}$ ph/s) to investigate collective excitations with energies

comparable to the characteristic energy scales near the Fermi level (<50 meV) — e.g., the superconducting gap and pseudogap in high-T_c cuprate superconductors. However, the full impact of RIXS has been substantially limited by the spectral flux (ph/s/meV) available from present X-ray sources lacking longitudinal coherence. High repetition rate seeded XFELs are anticipated to drive a qualitative advance in RIXS applications to quantum materials by providing $>10^{15}$ ph/s/meV from the source.

23.4.2 Collective Excitations: Transient Fields and Time-Dependent (Pump-Probe) Approaches

Time-domain approaches provide an important new window to understand collective excitations, potentially leading to the control of quantum phases and emergent properties by exploiting coherent light-matter interactions. Especially important is the ability to drive materials directly on the low energy scales at which fundamental excitations are found, *e.g.* phonons, plasmons, magnons or other collective modes. While many conventional probes have been applied to study the behaviour of these excitations as quasi-static parameters have been tuned (e.g. phase transitions mediated by temperature, pressure, or doping), their nonlinear response has not been studied in detail. Ultrafast pulses spanning the visible-to-THz regimes are effective stimuli of coherent collective excitations and can temporally alter the strongly intertwined degrees of freedom. For example, recent studies have shown that broadband THz pulses can selectively couple to electronic order, and thereby transiently decouple charge and lattice modes.[48] Such approaches can also trigger phase transitions and create new phases that are inaccessible in thermal equilibrium.[49-52] Tailored ultrafast vibrational excitation has been shown to drive insulator-to-metal phase transitions in colossal magnetoresistive manganites,[53] photo-induced superconductivity has been reported,[49] and enhanced superconductivity is claimed to result from transiently-driven nonlinear lattice dynamics in YBCO[54] and K-doped C_{60}.[55]

These novel photo-induced phenomena are ultimately related to the mechanisms of emergent phenomena in equilibrium and are a key step towards active control of material properties, yet a clear interpretation and characterization of the collective modes in the transient regime is still lacking. To date, time-resolved mid-IR spectroscopy provides information about the charge channel (e.g. optical conductivity and interlayer Josephson plasma resonance), but microscopic

information of the underlying degrees of freedom and their coupling is still lacking. Crucial pieces of information can be provided by time- and momentum-resolved RIXS. For example, in the case of photo-enhances superconductivity in cuprates, time-resolved RIXS at the Cu L-edge can map the evolution of magnetic excitations and phonons in time, energy, and momentum to provide a more complete microscopic picture about the transient superconducting phase. Furthermore, the time-evolution of charge-stripe order, a co-existing state in superconducting cuprates, and its associated excitations can be simultaneously monitored. This will provide new insights into the much-debated issue of the role of charge order in high-T_C superconductivity. This approach is applicable to many other outstanding problems in cuprates, such as the relation of recently discovered collective modes near the zone center and the role of magnetic fluctuations in the electron-doped cuprates.[56]

23.4.3 LCLS Instrument NEH 2.1

A new LCLS RIXS instrument, NEH 2.1,[26] is now under development to support the following areas of science: (1) q-resolved mapping of collective excitations in complex materials at the <30 meV scale, and over a range of scattering angles $2\theta = 40$ to 160 degrees (2) time-resolved RIXS of nonquillibrium materials and excited-state molecules (liquid or gas phase) at close to the Fourier-transform limit. The tuning range of NEH 2.1 will span from 0.25 to 1.6 keV covering the K-edges of light elements, C (284 eV), N (410 eV), O (543 eV) through the L-edges of the $3d$ transition metals, and extending into the lanthanide $M_{4,5}$-edges. The instrument will be served by the SXU source, and will share the same monochromator with instrument NEH 2.2 with adjustable resolving power from R = 10,000 to 50,000 near the Fourier transform limit. NEH 2.1 will provide an adjustable focus, as small as ~1.5 μm (horiz.) × 1.5 μm (vert.), and more typically with a small focus in one dimension (10 μm) compatible with high spectrometer resolution and a larger focus in the other dimension (400 μm) to exploit the large photon flux from the source, while mitigating the fluence (ph/cm^2) on the sample.

The RIXS spectrometer will incorporate varied line-spacing (VLS) gratings and high-pitch 2D detector to provide a resolving power of 50,000, for a combined (monochromator and spectrometer) resolving power of 30,000 at 1 keV (and higher at lower photon energies). A second VLS grating in the spectrometer will provide a resolving power of 10,000 to 20,000 with

much higher throughput for experiments requiring higher time resolution. The spectrometer will be designed to accommodate polarization analysis of the scattered photons using multilayer mirrors.

While the primary instrument of NEH 2.1 will be RIXS, space will be allocated (downstream of the RIXS sample chamber) for a roll-up endstation for high-resolution photoemission spectroscopy. This instrument will be used as a diagnostic tool for commissioning and calibration of the beamline monochromator, and as
a standalone endstation for time- and angle-resolved photoemission studies.

An important consideration in the application of XFELs to high-resolution RIXS is that the probe pulse does not disrupt the system under investigation. This is equally true for systems in a correlated ground state, and for systems prepared in a perturbative near-equilibrium excited state by a tailored excitation pulse. The X-ray probe interaction with the material under study must remain in the linear regime, and this places restrictions on the tolerable pulse fluence for ultrafast probes. Studies of nonlinear X-ray interactions with XFELs provide useful reference points. For example, XES measurements on Si samples at FLASH indicate an acceptable upper pulse fluence limit on the order of 10 mJ/cm^2.[57] Resonant diffraction studies of charge ordering in nickelate samples at LCLS indicate a safe upper bound of ~1 mJ/cm^2. For typical materials, these fluence levels correspond to ~0.1 eV/atom, and are consistent with ultrafast visible spectroscopy research over the past several decades, where the importance of maintaining a linear probe interaction is well established. For 1 keV photons and characteristic spot sizes ~2×10^{-5} cm^2 (e.g. 10 μm × 200 μm), this corresponds to a conservative upper limit on the usable fluence of ~10^8 ph/pulse or ~10^{14} ph/s at 1 MHz. Sample heating or other degradation effects may further limit the usable flux, or may require mitigation via sample rastering or replacement. However, a simple 1D model predicts only modest sample heating (~10 K) from a 20 mW X-ray beam incident at 20 degrees on a 100 μm thick sample with thermal conductivity of 20 W/K/m in contact with a cold head at 100K. Thus, high repetition rate XFEL sources offer tremendous potential for RIXS studies at the 10 meV scale.

23.5 Coherent imaging at the nanoscale

One of the original scientific visions for XFELs is the ability to image non-crystalline and non-identical structures via X-ray scattering with individual femtosecond pulses. X-ray pulses of sufficient intensity and short duration, can produce measurable and interpretable scattering patterns before the effects of X-ray induced sample damage dominate and degrade the scattering and achievable resolution.[58] Initial single particle imaging experiments at LCLS have produced single-shot coherent diffraction images of viruses,[59] bacteriophages,[60] organelles,[61] and cyanobacteria[62] to name a few. First data sets have been assembled into three dimensional images.[63] In addition to biological systems, single shot diffractive imaging has been used to study the morphology of aerosols,[64] power density dependent damage processes in atomic clusters,[65] and superfluid quantum systems.[66]

23.5.1 Single Particle Imaging

Important opportunities for single particle imaging include the investigation of proteins that do not readily crystalize, and the possibility to image the spontaneous dynamics of macromolecules and assemblies at physiological temperatures in their native environment. The capability to capture 10^8 to 10^{10} scattering snapshots per day exploiting high repetition rate XFELs will provide a qualitative advance in mapping the energy landscapes traversed by biological nanomachines – following their dynamics from the shortest timescales of bond-breaking to long timescales of large conformational changes. Results from cryogenic electron microscopy (cryo-EM) demonstrate that it is possible to extract three-dimensional structure,[67] conformational movies, and energy landscapes from experimental ultralow-signal snapshots of biological entities cryo-trapped in unknown orientations at unknown points in their work cycle.[68] The richness of a conformational movie and the detail with which an energy landscape can be mapped depend critically on the number of available snapshots. High repetition rate XFELs will enable major advances by providing an unprecedented number of snapshots of biological nanomachines in near-native environments.

The optimum conditions for single shot particle imaging are the subject of much active research. Biological samples are typically weak scatterers, leading to snapshots with low signal-to-noise ratios. There is evidence suggesting that the optimum region for single particle imaging is in the tender X-ray range between 2 keV and 6 keV, which may represent the best compromise

between scattering cross-section and resolution.[27] Sample heterogeneity combined with the low number of snapshots (at present low repetition rates) further complicates the assembly of complete data sets. Sample injection techniques need to be refined for the delivery of high-concentration of particles while minimizing background scattering. In order to address these challenges, LCLS has developed a roadmap towards single particle imaging with 3 Å resolution[69] and launched the Single Particle Imaging (SPI) initiative, consisting of 100 scientists from 20 institutions spanning eight countries. The initiative covers all aspects of SPI, from ultrafast X-ray induced damage processes to sample delivery and algorithm development. Recently, the SPI initiative reported X-ray scattering to ~6 Å from rice dwarf virus particles.[70]

23.5.2 LCLS Instrument NEH 1.2

A new LCLS instrument, NEH 1.2 (TXI),[26] is now under development to support a wide range of science in the tender X-ray range including: (1) coherent X-ray diffractive imaging as described above, (2) small angle X-ray scattering (SAXS), fluctuation SAXS, and time-resolved SAXS, (3) serial femtosecond crystallography with native phasing, e.g. S or P, (4) time-resolved X-ray emission spectroscopy, (5) time-resolve ambient-pressure photoemission spectroscopy. NEH 1.2 will have the unique feature of combining beams from independent undulators (SXU and HXU) at a crossing angle of ~96 mrad, to enable novel X-ray pump and X-ray probe studies.

{Fig 23.11 near here}

Figure 23.11 Conceptual layout of the proposed NEH 1.2 (TXI) instrument showing the optical layout, sample environment and X-ray detection. Photon beam direction from left to right. Soft X-ray offset mirror system (SOMS) and hard X-ray offset mirror system (HOMS) are flat mirrors and the soft X-ray (SXR) and hard X-ray (HXR) KB optics provide horizontal and vertical focusing (figure courtesy of P. Montanez, LCLS).

With the CW-SCRF linac at high repetition rates up to 1 MHz, the tuning range of the SXU branch of NEH 1.2 will span from 0.25 to 1.3 keV covering the K-edges of critical light elements, C (284 eV), N (410 eV), O (543 eV) through the L-edges of the $3d$ transition metals. The tuning range of the HXU branch will span the tender X-ray range from 1.0 to 5.0 keV covering the K-edges of P, S, and Cl. X-ray pulse energies range from ~1 mJ to ~100 μJ, depending on repetition rate and photon energy.[4, 5] With the Cu-RF linac (120 Hz repetition rate) the SXU branch will span from 0.25 to 5.0 keV, with X-ray pulse energies of ~8 mJ at 3.0 keV.

The HXU branch will span from 1.0 to 7.0 keV with X-ray pulse energies of ~3 mJ. Independent KB optics for the SXU and HXU branches will provide an adjustable focus as small as 1 μm diameter (FWHM).

The high peak pulse intensities achievable from the SXU with the Cu-RF linac will enable single shot snapshots of biological specimen with high contrast and nanometer resolution. Conversely, using the high repetition rate of the CW-SCRF linac will provide an unprecedented number of snapshots (at lower signal-to-noise ratios) that can then be used to reconstruct energy landscapes and conformational pathways.

In addition to X-ray scattering capabilities, NEH 1.2 will support time-resolved spectroscopy in the tender X-ray range via either absorption or emission using a tender X-ray emission spectrometer. It will further support novel nonlinear X-ray pump and X-ray probe applications as described in Section 23.2.2. NEH 1.2 has future potential to support dedicated endstations for time-resolved ambient-pressure photoemission and related applications in the tender X-ray range.

23.6 Conclusion

The next phase in the rapid development of XFELs will exploit continuous-wave superconducting accelerator technology to provide ultrafast X-ray pulses at high repetition rate (~MHz) in a uniform or programmable time structure. This development is driven by important new science opportunities that have been identified and advanced over the past decade through scientific workshops, both in the U.S. and around the world. In particular, the LCLS upgrade project (LCLS-II) will provide ultrafast X-rays in the 0.25-5.0 keV range at repetition rates up to 1 MHz with two independent XFELs based on adjustable-gap undulators: 0.25-1.25 keV soft X-ray undulator (SXU) and 1-5 keV hard X-ray undulator (HXU).[4, 5] In this chapter we have highlighted a few of the important new science opportunities enabled by such a facility in the areas of: (1) fundamental charge and energy flow in molecular complexes, (2) photo-catalysis and coordination chemistry, (3) quantum materials, and (4) coherent imaging at the nanoscale. The examples in this chapter represent just a few of the many science opportunities where high repetition rate is particularly enabling. Some key new experimental methods enabled by high

repetition rate are also described, and initial concepts and capabilities of new instrumentation being planned for the LCLS upgrade are outlined. Many of the new capabilities and experiments described here are critical for the grand science challenges related to energy and environment.

Acknowledgement

References

1. V. Ayvazyan, N. Baboi, J. Bähr, V. Balandin, et al., *Eur. Phys. J. D*, 2006, **37**, 297-303.
2. C. Bostedt, S. Boutet, D. M. Fritz, Z. Huang, et al., *Reviews of Modern Physics*, 2016, **88**, 015007.
3. I. Schlichting, W. E. White and M. Yabashi, eds., *Journal of Synchrotron Radiation: Special issue on X-ray Free-Electron Lasers, 22, 3*, 2016.
4. *New Science Opportunities enabled by LCLS-II X-ray Lasers*, SLAC-R-1053 (2015) https://portal.slac.stanford.edu/sites/lcls_public/Documents/LCLS-IIScienceOpportunities_final.pdf.
5. *LINAC Coherent Light Source II (LCLS-II) Project Final Design Report - LCLSII-1.1-DR-0251-R0*, SLAC National Accelerator Laboratory, https://slacspace.slac.stanford.edu/sites/lcls/lcls-2/fdr/pages/default.aspx, 2015.
6. R. Dörner, V. Mergel, O. Jagutzki, L. Spielberger, et al., *Physics Reports*, 2000, **330**, 95-192.
7. J. Ullrich, R. Moshammer, A. Dorn, R. Dörner, et al., *Rep. Prog. Phys.*, 2003, **66**, 1463.
8. A. Landers, T. Weber, I. Ali, A. Cassimi, et al., *Phys. Rev. Lett.*, 2001, **87**, 013002.
9. J. B. Williams, C. S. Trevisan, M. S. Schöffler, T. Jahnke, et al., *Phys. Rev. Lett.*, 2012, **108**, 233002.
10. A. Rudenko and D. Rolles, *J. Electron. Spectrosc. Relat. Phenom.*, 2015, **204, Part B**, 228-236.
11. S. Zeller, M. Kunitski, J. Voigtsberger, A. Kalinin, et al., *Proceedings of the National Academy of Sciences*, 2016, **113**, 14651-14655.
12. K. Schnorr, A. Senftleben, M. Kurka, A. Rudenko, et al., *Phys. Rev. Lett.*, 2013, **111**, 093402.
13. K. Schnorr, A. Senftleben, M. Kurka, A. Rudenko, et al., *Phys. Rev. Lett.*, 2014, **113**, 073001.
14. B. Erk, R. Boll, S. Trippel, D. Anielski, et al., *Science*, 2014, **345**, 288-291.
15. M. P. Minitti, J. M. Budarz, A. Kirrander, J. S. Robinson, et al., *Phys. Rev. Lett.*, 2015, **114**, 255501.

16. B. K. McFarland, J. P. Farrell, S. Miyabe, F. Tarantelli, et al., *Nature Communications*, 2014, **5**, 4235.
17. M. Pitzer, M. Kunitski, A. S. Johnson, T. Jahnke, et al., *Science*, 2013, **341**, 1096-1100.
18. S. Tanaka and S. Mukamel, *Phys. Rev. Lett.*, 2002, **89**, 043001.
19. J. D. Biggs, Y. Zhang, D. Healion and S. Mukamel, *Proceedings of the National Academy of Sciences*, 2013, **110**, 15597-15601.
20. I. V. Schweigert and S. Mukamel, *Phys. Rev. Lett.*, 2007, **99**, 163001.
21. W. Hua, K. Bennett, Y. Zhang, Y. Luo, et al., *Chemical Science*, 2016, **7**, 5922-5933.
22. S. Mukamel, D. Abramavicius, L. Yang, W. Zhuang, et al., *Acc. Chem. Res.*, 2009, **42**, 553-562.
23. X. Li, T. Zhang, C. N. Borca and S. T. Cundiff, *Phys. Rev. Lett.*, 2006, **96**, 057406.
24. T. Brixner, J. Stenger, H. M. Vaswani, M. Cho, et al., 2005, **434**, 625-628.
25. M. O. Krause and J. H. Oliver, *J. Phys. Chem. Ref. Data*, 1979, **8**, 329-338.
26. *LCLS Strategic Development Plan* (2015), https://portal.slac.stanford.edu/sites/lcls_public/Documents/LCLS_Strategic_Developme nt_Plan.pdf.
27. M. Bergh, G. Huldt, N. Tîmneanu, F. R. N. C. Maia, et al., *Quarterly Reviews of Biophysics*, 2008, **41**, 181-204.
28. A. A. Zholents and W. M. Fawley, *Phys. Rev. Lett.*, 2004, **92**, 224801.
29. A. Marinelli, D. Ratner, A. A. Lutman, J. Turner, et al., *Nat Commun*, 2015, **6**, 6369.
30. *APEX Experimental Results and Simulation Comparison*, https://docs.slac.stanford.edu/sites/pub/Publications/APEX_Experimental_Results and_Simulation_Comparison.pdf
31. S. E. Canton, K. S. Kjær, G. Vankó, T. B. van Driel, et al., *Nat Commun*, 2015, **6**, 6359.
32. P. Wernet, K. Kunnus, I. Josefsson, I. Rajkovic, et al., *Nature*, 2015, **520**, 78-81.
33. W. Witczak-Krempa, G. Chen, Y. B. Kim and L. Balents, *Annual Review of Condensed Matter Physics*, 2014, **5**, 57-82.
34. E. Dagotto, *Science*, 2005, **309**, 257-262.
35. X.-L. Qi and S.-C. Zhang, *Reviews of Modern Physics*, 2011, **83**, 1057-1110.
36. M. Z. Hasan and C. L. Kane, *Reviews of Modern Physics*, 2010, **82**, 3045-3067.
37. S. Mühlbauer, B. Binz, F. Jonietz, C. Pfleiderer, et al., *Science*, 2009, **323**, 915-919.
38. E. S. Reich, *Nature*, 2012, **492**, 165.
39. Y. Zhu and H. Durr, *Phys. Today*, 2015, **68**, 32.
40. L. J. P. Ament, M. van Veenendaal, T. P. Devereaux, J. P. Hill, et al., *Reviews of Modern Physics*, 2011, **83**, 705-767.
41. M. Guarise, B. Dalla Piazza, M. Moretti Sala, G. Ghiringhelli, et al., *Phys. Rev. Lett.*, 2010, **105**, 157006.
42. M. Le Tacon, G. Ghiringhelli, J. Chaloupka, M. M. Sala, et al., *Nat Phys*, 2011, **7**, 725-730.
43. J. Schlappa, T. Schmitt, F. Vernay, V. N. Strocov, et al., *Phys. Rev. Lett.*, 2009, **103**, 047401.
44. J. Schlappa, K. Wohlfeld, K. J. Zhou, M. Mourigal, et al., *Nature*, 2012, **485**, 82-85.
45. W. S. Lee, S. Johnston, B. Moritz, J. Lee, et al., *Phys. Rev. Lett.*, 2013, **110**, 265502.
46. *ESRF ID-32 soft X-ray spectroscopy beamline*, http://www.esrf.eu/ID32
47. *NSLS-II Soft Inelastic X-ray Scattering (SIX) Beamline (2-ID)*, https://www.bnl.gov/ps/beamlines/beamline.php?b=SIX

48.   M. Porer, U. Leierseder, J. M. Ménard, H. Dachraoui, et al., *Nat Mater*, 2014, **13**, 857-861.

49.   D. Fausti, R. I. Tobey, N. Dean, S. Kaiser, et al., *Science*, 2011, **331**, 189-191.

50.   F. Schmitt, P. S. Kirchmann, U. Bovensiepen, R. G. Moore, et al., *Science*, 2008, **321**, 1649-1652.

51.   J. P. Hinton, J. D. Koralek, Y. M. Lu, A. Vishwanath, et al., *Phys. Rev. B*, 2013, **88**, 060508.

52.   L. Stojchevska, I. Vaskivskyi, T. Mertelj, P. Kusar, et al., *Science*, 2014, **344**, 177-180.

53.   M. Rini, R. Tobey, N. Dean, J. Itatani, et al., *Nature*, 2007, **449**, 72-74.

54.   R. Mankowsky, A. Subedi, M. Forst, S. O. Mariager, et al., *Nature*, 2014, **516**, 71-73.

55.   M. Mitrano, A. Cantaluppi, D. Nicoletti, S. Kaiser, et al., *Nature*, 2016, **530**, 461-464.

56.   W. S. Lee, J. J. Lee, E. A. Nowadnick, S. Gerber, et al., *Nat Phys*, 2014, **10**, 883-889.

57.   M. Beye, S. Schreck, F. Sorgenfrei, C. Trabant, et al., *Nature*, 2013, **501**, 191-194.

58.   R. Neutze, R. Wouts, D. v. d. Spoel, E. Weckert, et al., *Nature*, 2000, **406**, 752-757.

59.   M. M. Seibert, T. Ekeberg, F. R. N. C. Maia, M. Svenda, et al., *Nature*, 2011, **470**, 78-U86.

60.   S. Kassemeyer, J. Steinbrener, L. Lomb, E. Hartmann, et al., *Opt. Express*, 2012, **20**, 4149-4158.

61.   M. F. Hantke, D. Hasse, F. R. N. C. Maia, T. Ekeberg, et al., *Nature Photonics*, 2014, **8**, 943-949.

62.   G. van der Schot, M. Svenda, F. R. N. C. Maia, M. Hantke, et al., *Nat Commun*, 2015, **6**, 5704.

63.   T. Ekeberg, M. Svenda, C. Abergel, F. R. N. C. Maia, et al., *Phys. Rev. Lett.*, 2015, **114**, 098102.

64.   N. D. Loh, C. Y. Hampton, A. V. Martin, D. Starodub, et al., *Nature*, 2012, **486**, 513-517.

65.   H. Thomas, A. Helal, K. Hoffmann, N. Kandadai, et al., *Phys. Rev. Lett.*, 2012, **108**, 133401.

66.   L. F. Gomez, K. R. Ferguson, J. P. Cryan, C. Bacellar, et al., *Science*, 2014, **345**, 906-909.

67.   J. Frank, *Three-Dimensional Electron Microscopy of Macromolecular Assemblies*, 2nd edn., Oxford University Press, New York, 2006.

68.   A. Dashti, P. Schwander, R. Langlois, R. Fung, et al., *P Natl Acad Sci USA*, 2014, **111**, 17492-17497.

69.   A. Aquila, A. Barty, C. Bostedt, S. Boutet, et al., *Struct. Dyn.*, 2015, **2**, 041701.

70.   A. Munke, J. Andreasson, A. Aquila, S. Awel, et al., *Scientific Data*, 2016, **3**, 160064.
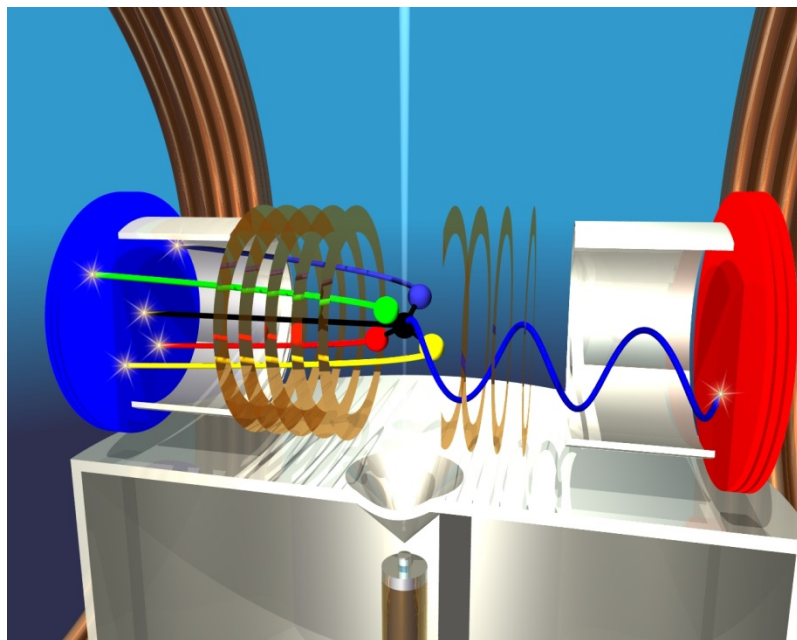
Figure Captions

Figure 23.1 Artist view of a molecular reaction microscope (also known as COLd Target Recoil Ion Momentum Spectroscopy, COLTRIMS). Only one molecule is in the X-ray beam on each pulse (i.e. less than one ionization event per pulse). The ion and electron momenta are fully characterized in coincidence via position-sensitive time-of-flight detectors (graphic courtesy of R. Dörner, Goethe U. Frankfurt).
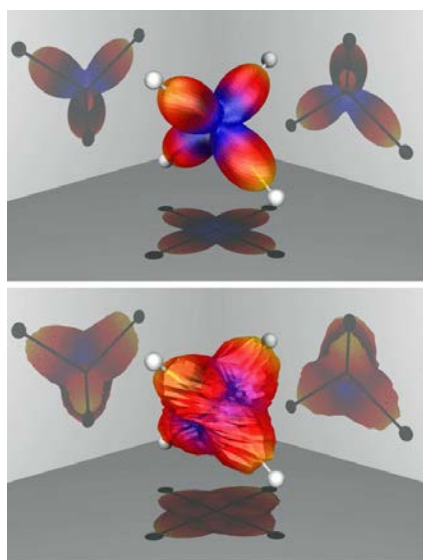
Figure 23.2 Methane (stationary electronic ground-state) imaged in the molecular frame via the K-shell photoelectron angular distribution. Top: Calculated photoelectron angular distribution integrated over all polarization directions. Bottom: The experimental photoelectron angular distribution obtained from the (H^+, H^+, CH^{+2}) decay pathway (from [9]).
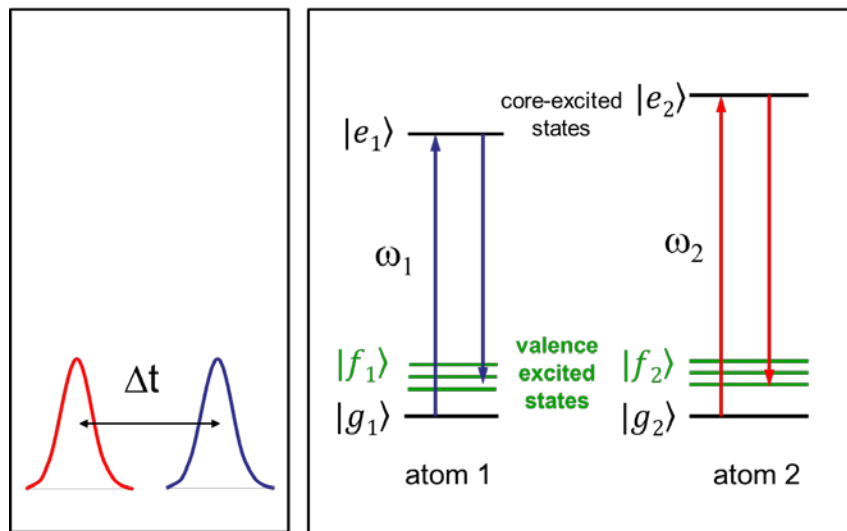
Figure 23.3 Illustration of coherent or Stimulated X-ray Raman Spectroscopy (SXRS) in which localized valence excitations $|f_1\rangle$ and $|f_2\rangle$ are created and probed via resonant Raman processes at specific atoms. This approach creates a local valence excitation, and enables element-specific probing of charge flow.
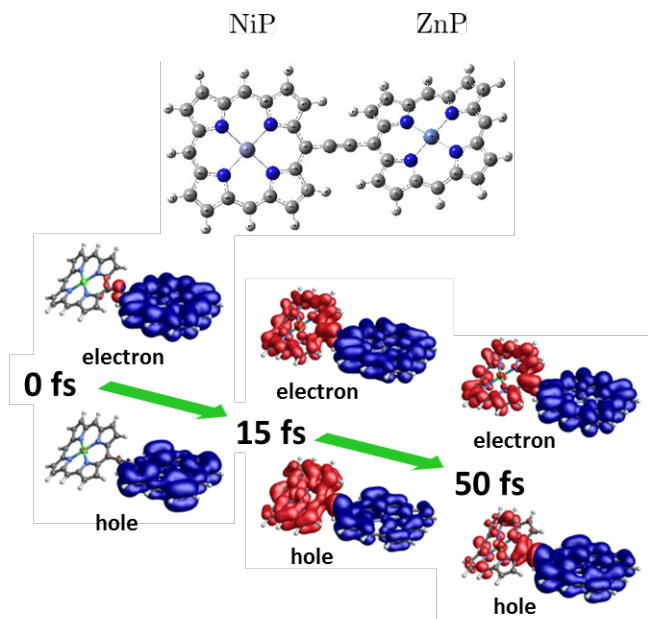
Figure 23.4 Excitation energy transfer simulation in Zn/Ni porphyrin heterodimer. The X-ray pump pulse is resonant with the Zn L_3-edge, and creates a localized valence excitation (wavepacket) via SXRS. Evolution of electron and hole densities (isosurfaces) are calculated from the non-stationary valence superposition states prepared via SXRS (adapted from ref. 19).
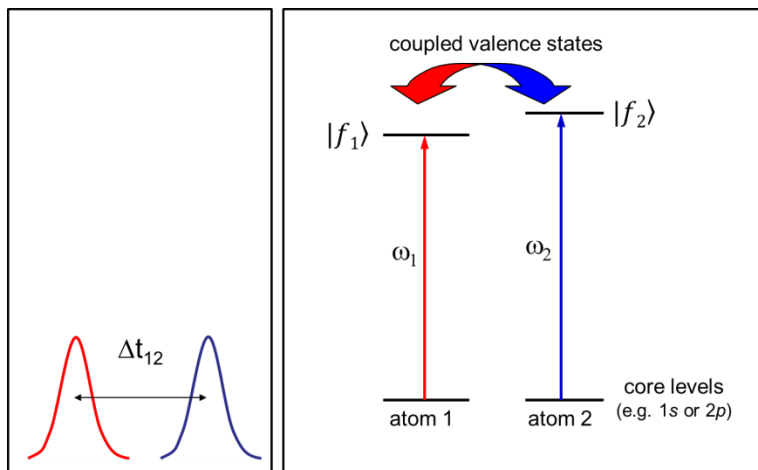

Figure 23.5 Illustration of core-hole correlation spectroscopy in which resonant core-level excitation of two atoms is used to probe the coupling between their respective valence states f_1 and f_2.[20]

Figure 23.6 Valence and core-excited states of aminophenols of *para* and *ortho* isomers of aminophenol, and the predicted corresponding 2D X-ray core-hole correlation maps. The off-diagonal cross-peaks (right map) indicate the quantum mixing between nitrogen- and oxygen-

associated valence states (mixing of the N-1s and O-1s XANES spectra). Such quantum effects are absent in the para isomer due to the separation of the O and N atoms (adapted from ref. 20).
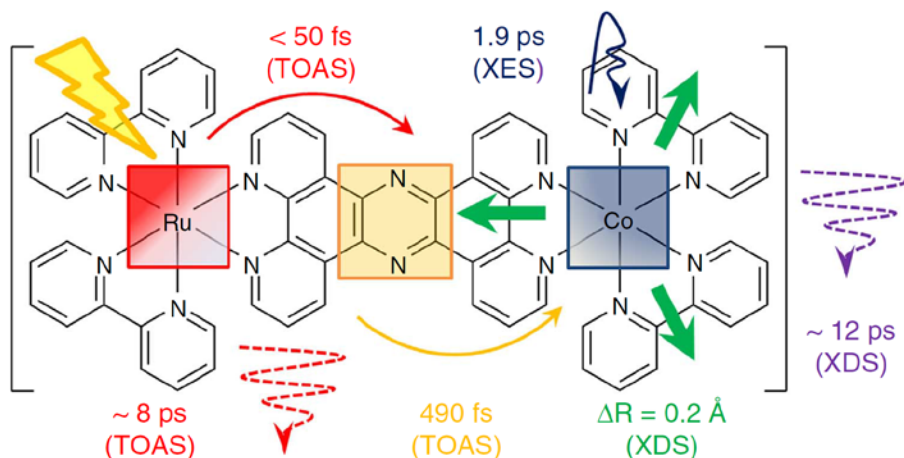

Figure 23.7 Non-equilibrium electron-transfer across the photoexcited (^{1}Ru^{II}=^{1}Co^{III}) model photo-catalyst. The fundamental timescales are indicated, as obtained from transient optical absorption spectroscopy (TOAS), X-ray emission spectroscopy (XES), and X-ray diffuse scattering (XDS).[31]
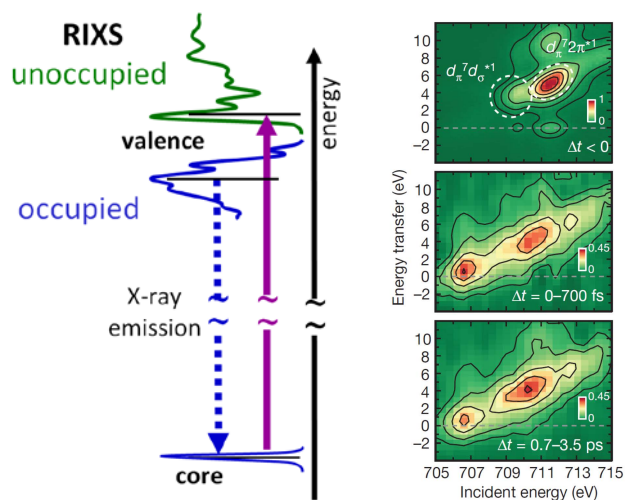

Figure 23.8 Left: Resonant inelastic X-ray scattering (RIXS). Right: Time-resolved Fe L$_3$-RIXS maps (energy transfer vs. incident photon energy) of Fe(CO)$_5$ ground-state (top), and difference intensities for the time intervals 0-700 fs (middle) and 0.7-3.5 ps (bottom).[32]
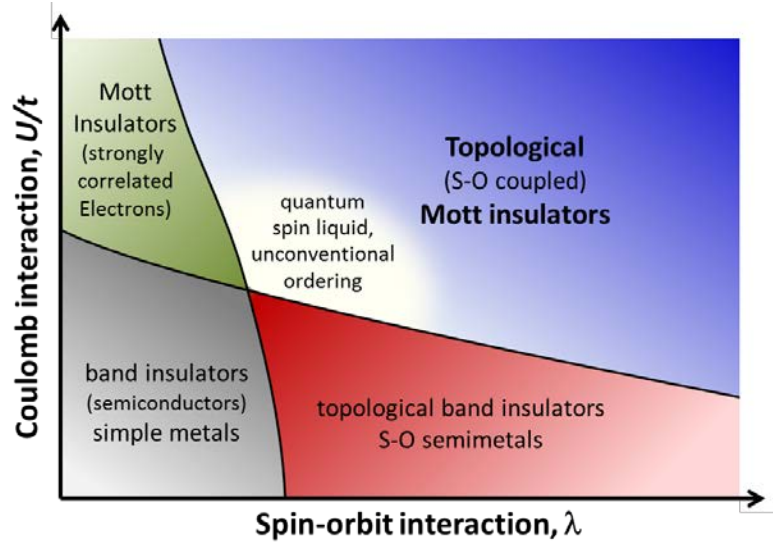
Figure 23.9 Classification of materials via spin-orbit coupling and Coulomb interaction strength (adapted from ref. 33).
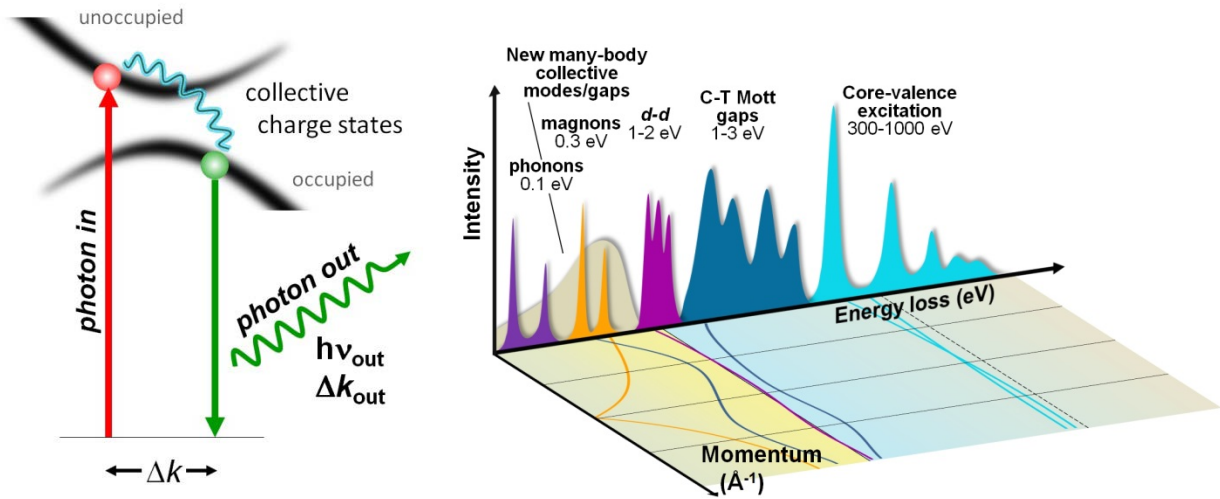

Figure 23.10 Left: Resonant inelastic X-ray scattering (RIXS) probe of collective charge states. Right: Collective excitations that can be characterized by RIXS – including excitations within *d*-orbital manifolds (*d-d*) and charge-transfer excitations (CT). Higher resolution is essential to reveal collective excitations at energy scales comparable to that of superconducting gap and pseudogap ~k_BT (<25 meV) (image adapted from ref. 39).
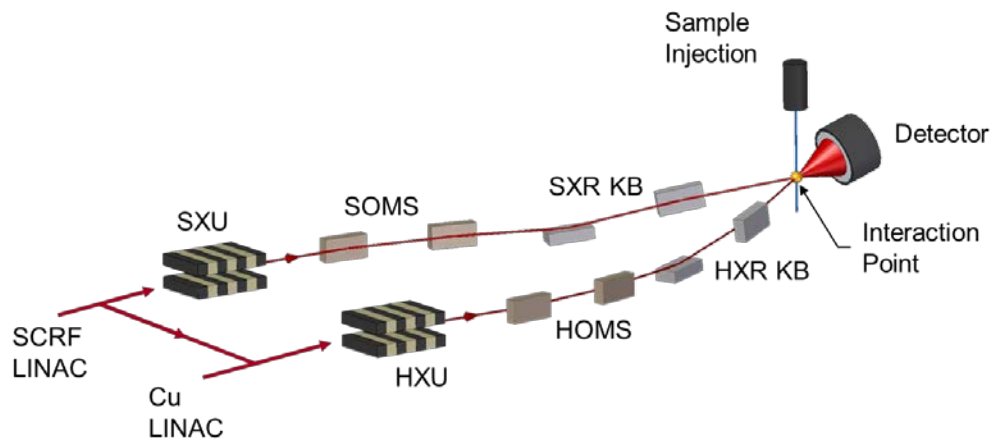
Figure 23.11 Conceptual layout of the proposed NEH 1.2 (TXI) instrument showing the optical layout, sample environment and X-ray detection. Photon beam direction from left to right. Soft X-ray offset mirror system (SOMS) and hard X-ray offset mirror system (HOMS) are flat mirrors and the soft X-ray (SXR) and hard X-ray (HXR) KB optics provide horizontal and vertical focusing (figure courtesy of P. Montanez, LCLS).